Title

Capacity loss of non-aqueous Li-Air battery due to insoluble product formation: Approximate solution and experimental validation

Authors

Yuan, Hao
Read, Jeffrey A
Wang, Yun

Publication Date

2019-12-01

DOI

10.1016/j.mtener.2019.100360

Peer reviewed

Materials Today Energy 14 (2019) 100360

Contents lists available at ScienceDirect

Materials Today Energy

journal homepage: www.journals.elsevier.com/materials-today-energy/

Capacity loss of non-aqueous Li-Air battery due to insoluble product formation: Approximate solution and experimental validation

Hao Yuan [a], Jeffrey A. Read [b], Yun Wang [a, *]

[a] Renewable Energy Resources Lab (RERL), Department of Mechanical and Aerospace Engineering, University of California, Irvine, CA 92697-3975, United States

[b] US Army Research Laboratory, Electrochemistry Branch, Sensors and Electron Devices Directorate, Adelphi, MD 20783-1138, USA

ARTICLE INFO

Article history:
Received 1 August 2019
Received in revised form
2 October 2019
Accepted 11 October 2019
Available online xxx

Keywords:
Lithium-air battery
Air cathode
Capacity loss
Approximate solution
Experiment

ABSTRACT

In this paper, we present a study of Lithium (Li)-air battery capacity by accounting for the voltage loss associated with the electrode passivation and transport resistance caused by insoluble product formation. Two regimes are defined, in which approximate formulas are developed to explicitly evaluate the battery capacity, along with extensive validation against experimental data of various cathode properties and materials from our and several other groups. The dependence of battery capacity on the surface coverage factor, tortuosity, and Damköhler numbers (Da) is explicitly expressed and discussed. The formulas provide a guideline for experimentalists and practitioners in air cathode design, analysis, and control.

Published by Elsevier Ltd.

1. Introduction

Li-air batteries have received a growing rearch attention in recent years [1]. A major advantage of the Li-air battery is its high specific energy, which measures the amount of energy per unit weight and is 11,680 Wh/kg for the lithium metal anode, comparable to that of gasoline [2]. This is several times higher than conventional Li-ion batteries, making Li-air batteries a candidate of next generation energy storage devices [3,4]. Besides specific energy, the technology also offers promising potentials for high rechargeability, long cycling life, and high energy efficiency [5]. Visco et al. reported the theoretical storage values of non-aqueous and aqueous electrolyte Li-air batteries to be 3405 Wh/kg and 3850 Wh/kg, respectively [6]. Ideally, a Li-air battery discharges until exhausting all the available oxygen or Li metal. The electrochemistry can be reversible, and the rechargeable Li-air battery has been investigated intensively [7–11]. However, its practical capacity at current stage is much smaller than the theoretical values. A major limitation arises from the air cathode of the battery, where insoluble discharge products such as Li_2O_2, Li_2CO_3, and Li_2O accumulate at the reaction sites inside the porous structure. These insoluble products are very low in electron conductivity, leading to electrode passivation. In another word, presence of these discharge products will significantly raise the transport resistance for electron access to the reaction interface, leading voltage loss. In addition, their physical presence raises the oxygen transport polarization by narrowing down the pore passages where dissolved oxygen transport takes place [12].

Fig. 1 schematically shows a Li-air battery and its discharge operation. In general, the Li ions and electrons are produced in the anode as Li is oxidized during discharge. The Li ions migrate via the electrolyte to the cathode, where they combine with oxygen and electrons to form Li compounds. Electric work is produced when electrons travel the external circuit. In charging, Li ions are plated at the anode with oxygen released in the cathode. In air cathodes, the pore networks provide pathways for transporting Li ions and oxygen in the electrolyte, while the carbon structure conducts electrons. At the reaction surface where all the reactants are accessible, Li oxides are produced as discharge product, which are usually insoluble in the major set of nonaqueous electrolytes and thus precipitate in local pores hampering the transport of reactants (Li ions and oxygen). Li oxide deposits are generally low in electronic conductivity, thus their coverage over the reaction surface limits

* Corresponding author. Renewable Energy Resources Lab (RERL), Department of Mechanical and Aerospace Engineering, University of California, Irvine, CA 92697-3975, United States. Fax: +1 949-824-8585
E-mail address: yunw@uci.edu (Y. Wang).

https://doi.org/10.1016/j.mtener.2019.100360
2468-6069/Published by Elsevier Ltd.

Nomenclature

a	effective local surface area density
c	molar concentration, mol/m^3
D	species diffusivity, m^2/s
Da	Damköhler number
F	Faraday's constant, 96,487C/mol
I	current density, A/m^2
j	transfer current density, A/m^3
M	molecular weight, kg/mol
n	electrons number in the reaction
Q	charge capacity, C/m^2
R	universal gas constant, $8.314 J/mol{\cdot}K$
R_0	contact resistance, Ωm^2
r_c	dimension of carbon particle
s	volume fraction of insoluble product
t	time, s
T	temperature, K
u_x	velocity, m/s
u	energy capacity per area, J/m^2
V	Voltage, V

Greek

α	overpotential ratio
β	symmetry factor
δ	the cathode thickness, mm
ρ	density, kg/m^3
ε	volumetric porosity
η	surface overpotential, V
τ_a	surface effect factor
τ_d	tortuosity coefficient
τ	tortuosity factor

Superscripts and Subscripts

a	coverage loss
d	clogging loss
cut	cutoff state
eff	effective value
o_2	oxygen
prod	product
0	reference value; initial value

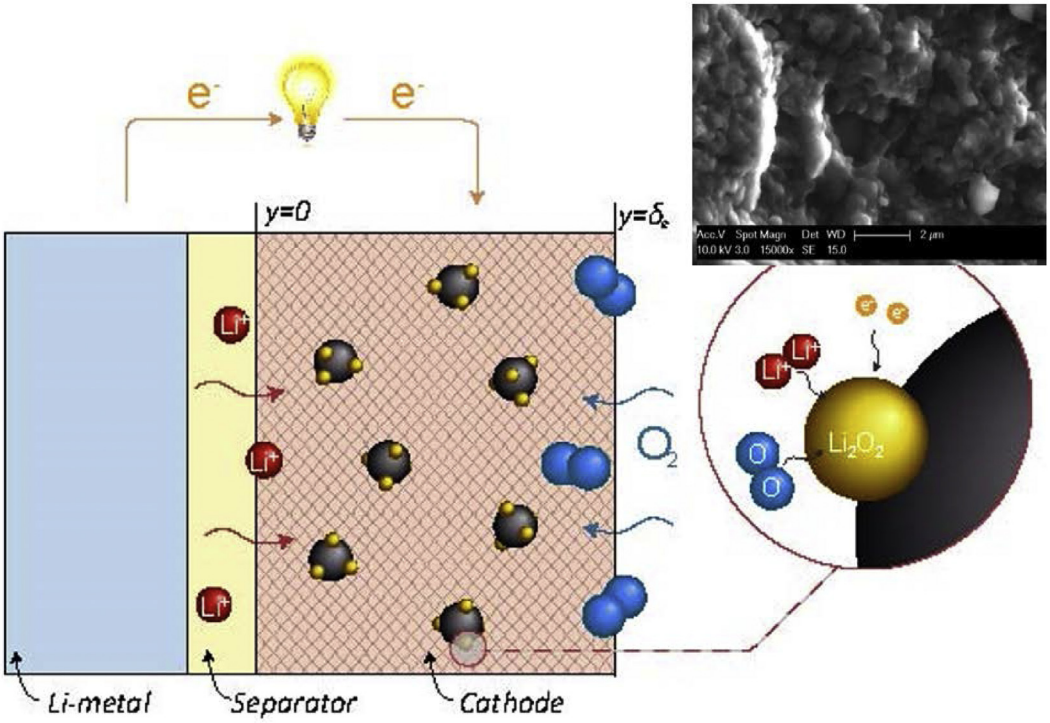

Fig. 1. Schematic of a Li-air battery and its discharge operation with Li_2O_2 as an example of discharge product [13].

access to the surface, causing electrode passivation. The passivation contributes to major voltage loss, reducing the cells discharge capability. Thus, the air cathode plays a major role in the voltage and the capacity of Li-Air cells in practice.

In modeling and analysis, Yuan et al. [14] discussed multiphase phenomena, solid product generation, and morphology growth in Li-air battery cathodes by focusing on the effective properties involving tortuosity factors, solid product morphologies, as well as effects on the void space clogging, surface area reduction and passivation. The paper provided an understanding of multiphase transport phenomena and implementation of the detailed models for precipitate formation and morphology growth in Li-air battery cathodes. Yoo et al. [15] developed a mathematical model to study the performance of Li-air batteries when a significant volume change occurs in the electrodes. They showed electrode passivation in the cathode depends highly on the solubility of cathode products. Viswanathan et al. [16] conducted electrochemical experiments using a reversible internal redox couple and employed a

metal-insulator-metal charge transport model to investigate the electrical conductivity through Li_2O_2 films produced during Li-air battery discharge. Both experiment and theory showed a "sudden death" in charge transport when the film thickness is about 5–10 nm. Sahapatsombut et al. [17] developed a macroscopic homogeneous model to evaluate the performance of a rechargeable nonaqueous Li-air battery. Sandhu et al. [18] developed a diffusion-limited transient model for lithium-air batteries to predict capacity. Both of them showed that the precipitated products have a significantly negative effect on oxygen transport to the reaction sites, limiting the Li-air batteries power density. Some works [19–21] indicated that the internal ohmic loss in the separator and solid electrolyte would further reduce power density. Chen et al. [22] investigated the performance of Li-air batteries with carbon nanotube and carbon nanofiber cathodes. They found that the discharge capacity is mainly limited by the combination of oxygen diffusion and electrical resistance of the discharge precipitate at the reaction surface. A mathematical model for the discharge of Li-air batteries was also developed to describe the effects of the finite conductivity of the deposit layer in the cathode. Christensen et al. [23] discussed how the deposition of electrically resistive precipitates limit battery capacity. Nemanick [24] investigated the electrochemistry of nonaqueous Li-oxygen batteries on both reduction and oxidation using carbon black and single-walled nanotube (SWNT) microcavity electrodes, showing that the oxygen reduction reaction (ORR) produces two electrochemically distinct Li_2O_2 species that can be differentiated by their behavior on charge. They pointed out that controlling the ratio of Li_2O_2 species can effectively reduce the overpotential on charge transfer. Yuasa et al. [25] investigated the discharge/charge performance of Li-air batteries using the carbon-supported $LaMn_{0.6}Fe_{0.4}O_3$ nanoparticle as the cathode catalyst. They revealed that oxygen diffusion into the air electrode strongly affects the discharge capacity. Andrei et al. [26] proposed a physics-based model for Li-air batteries, showing the specific capacity is mainly limited by the oxygen diffusion length. They also discussed various approaches to increase the specific capacity and the energy density of Li-air batteries.

Despite the above efforts in Li-air battery modeling, analytical models and approximate solutions are highly desirable in design and optimization of Li-air battery. In this paper, we derived analytical solution based on the Tafel equation, which is widely used to describe the oxygen reduction reaction (ORR) rate for Li-air battery and other electrochemical systems, and investigate the insoluble product's effects on battery capacity and relate the cathode structural properties to battery capacity. Extensive validation was carried out against experimental data of various porosities and cathode materials.

2. Modeling and analysis

In operation, the discharge insoluble Li oxides are produced and deposited at local reaction sites in the cathode. The initial precipitation likely occurs at preferred sites first, followed by thin film formation covering the reaction surface and resisting electron access. For porous electrodes, reduction in the effective surface area can be written by a geometric relation, such as the power law, to relate the deposit's volume fraction [27]:

$$a = a_0 \left(1 - \frac{\varepsilon_{prod}}{\varepsilon_0}\right)^{\tau_a} \tag{1}$$

where $\frac{\varepsilon_{prod}}{\varepsilon_0}$ is the volume fraction of insoluble precipitates in the pore space and τ_a denotes the coverage factor, measuring the degree of insoluble product effect on the reaction area. This empirical expression was also adopted to describe the impact of liquid water and ice on the electrochemical reaction surface in PEM fuel cells [28,49]. A similar expression was reported by others [29,30]:

$$a = a_0 \left[1 - \left(\frac{\varepsilon_{prod}}{\varepsilon_0}\right)^{\tau_a}\right] \tag{2}$$

ε_{prod} is calculated through the reaction rate via Faraday's law [26]:

$$\varepsilon_{prod} = \int_0^t \frac{j_c M_{prod}}{nF\rho_{prod}} dt = \varepsilon_{prod,0} + \frac{IM_{prod}}{n\delta F\rho_{prod}} t \tag{3}$$

where n denotes the moles of electrons transferred per mole of the product. For different Li oxides which is primarily determined by the electrolyte material, n and M_{prod} will be different. The surface effect factor τ_a also accounts for electrode passivation. For the spherical-film growth mode, the exponent coefficient τ_a is given by Ref. [31]:

$$\tau_a = -\frac{I(1-\beta)F}{a_0 RTln\left(1-\frac{\varepsilon_{prod}}{\varepsilon}\right)} \left\{ A_0 \left[\left(1 + \frac{\varepsilon_{prod}}{\varepsilon_0}\right)^{\frac{1}{3}} - 1 \right] r_c + R_0 \right\} \tag{4}$$

where A_0 is the proportional coefficient between the film resistance and thickness [32], and R_0 is the contact resistance between the carbon particle and deposit shell [31]. The above indicates that τ_a is proportional to the current density I and a function of ε_{prod}. In porous electrodes, various growth modes of insoluble products are encountered. The following correlation was proposed to account for the effects of current density and insoluble product volume fraction [31]:

$$\tau_a = \begin{cases} B_1 \dfrac{I}{I_0} & s < s_0 \\ \dfrac{I}{I_0}[B_1 + B_2(s - s_0)] & otherwise \end{cases} \tag{5}$$

where $s = \frac{\varepsilon_{prod}}{\varepsilon}$. Another effect of insoluble precipitates is to hamper oxygen transport: insoluble precipitates will narrow the oxygen transport passage in the pore structure, reducing the effective oxygen diffusivity. Assuming no porous structure in the precipitates, the effective oxygen diffusivity can be modified following the Bruggeman correlation [33]:

$$D_{eff,o2} = \varepsilon^{\tau_d} D_{0,o2} = \left(\varepsilon_0 - \varepsilon_{prod}\right)^{\tau_d} D_{0,o2} \tag{6}$$

where τ_d represents the tortuosity of the diffusion path. Another popular correlation is also applicable:

$$D_{eff} = \frac{\varepsilon}{\tau} D \tag{7}$$

For Eq. (6), the tortuosity factor is determined by the pore network [34]:

$$\tau_d = \begin{cases} 1.5 & (spheres) \\ 2 & (cylinders) \end{cases} \tag{8}$$

For fibrous paper and cloth, the tortuosity can be 3.0 and 1.1, respectively [35]. In addition, the MacMullin number (N_M) is also adopted to evaluate the effective diffusivity, implicitly defined as $\varepsilon^{-\tau_d}$ in Eq. (6). Table 2 lists the expression of N_M for various porous media as a function of ε.

For oxygen transport in cathode, the 1-D equation in the porous electrode can be written as [37,38]:

$$\frac{\partial \varepsilon C_{o2}}{\partial t}+\frac{\partial u_x C_{o2}}{\partial x}=\frac{\partial}{\partial x}\left(D_{eff,o2}\frac{\partial C_{O_2}}{\partial x}\right)+\frac{j_c}{4F} \tag{9}$$

In the absence of electrolyte bulk flow, the convection term can be neglected. Assuming quasi-steady-state operation and uniform reaction, the local oxygen concentration can be analytically obtained [39]:

$$\frac{C_{o2}(y)}{C_{o2,\delta}}=1-\mathrm{Da}\frac{1-\left(\frac{y}{\delta}\right)^2}{\varepsilon^{\tau_d-\tau_{d,0}}\left(1-\frac{\varepsilon_{prod}}{\varepsilon_0}\right)^{\tau_d}} \tag{10}$$

where dimensionless parameter Da is the Damköhler number, defined by:

$$\mathrm{Da}=\frac{I}{8F}\frac{\delta}{C_{O_{2,\delta}}D_{O_2}\varepsilon_0^{\tau_{d,0}}}=\frac{\text{reaction rate}}{\text{mass transport rate}} \tag{11}$$

The overpotential can be derived through Tafel equation, which is widely adopted to describe the rate of the oxygen reduction reaction (ORR) for Li-air battery [12,32] and fuel cells [27]:

$$j_c=-ai_c=-ai_{0,c}^{ref}C_{O^2}^{1-\beta}C_e^{1-\beta}exp\left(-\frac{1-\beta}{RT}F\eta\right) \tag{12}$$

and Eq. (10):

$$\Delta\eta'=\frac{RT}{(1-\beta)F}\left[\tau_a\ln\left(1-\frac{\varepsilon_{prod}}{\varepsilon_0}\right)+(1-\beta)\ln\left(1-\mathrm{Da}\frac{1-\left(\frac{y}{\delta}\right)^2}{\varepsilon^{\tau_d-\tau_{d,0}}\left(1-\frac{\varepsilon_{prod}}{\varepsilon_0}\right)^{\tau_d}}\right)\right]=\Delta\eta_a+\Delta\eta_d' \tag{13}$$

Note that $\Delta\eta_d'$ contains the oxygen transport voltage loss prior to formation of any precipitates in the cathode. To extract the voltage loss caused by discharge deposit only, we eliminate the portion of the oxygen transport voltage loss prior to formation of any precipitates by defining:

$$\Delta\eta=\frac{RT}{(1-\beta)F}\left[\tau_a\ln\left(1-\frac{\varepsilon_{prod}}{\varepsilon_0}\right)+(1-\beta)\ln\left(\frac{1-\mathrm{Da}\frac{1-\left(\frac{y}{\delta}\right)^2}{\varepsilon^{\tau_d-\tau_{d,0}}\left(1-\frac{\varepsilon_{prod}}{\varepsilon_0}\right)^{\tau_d}}}{1-\mathrm{Da}\frac{1-\left(\frac{y}{\delta}\right)^2}{\varepsilon^{\tau_d-\tau_{d,0}}}}\right)\right]=\Delta\eta_a+\Delta\eta_d \tag{14}$$

where,

$$\Delta\eta_a=\frac{RT\tau_a\ln\left(1-\frac{\varepsilon_{prod}}{\varepsilon_0}\right)}{(1-\beta)F} \tag{15}$$

$$\Delta\eta_d=\frac{RT}{F}\ln\left(\frac{1-\mathrm{Da}\frac{1-\left(\frac{y}{\delta}\right)^2}{\varepsilon^{\tau_d-\tau_{d,0}}\left(1-\frac{\varepsilon_{prod}}{\varepsilon_0}\right)^{\tau_d}}}{1-\mathrm{Da}\frac{1-\left(\frac{y}{\delta}\right)^2}{\varepsilon^{\tau_d-\tau_{d,0}}}}\right) \tag{16}$$

$\Delta\eta_a$ represents the voltage loss caused by electrode passivation and surface reduction, and $\Delta\eta_d$ denotes the voltage loss associated with the oxygen transport resistance and precipitates.

In addition, catalyst greatly improves the electrochemical reaction kinetics and Li-air battery performance by lowering the activation energy [40–43]. In modeling, catalyst's impact on the electrochemical reaction rate is taken into account through the exchange current density, see $i_{0,c}$ in Eq. (12).

For evaluation, the total voltage loss associated with the formation of insoluble products can be approximated by using the following equation:

$$\Delta\eta=\Delta\eta_a+\Delta\eta_d\left(\frac{y}{\delta}=\frac{1}{2}\right) \tag{17}$$

Assuming the voltage loss after the initial start is caused by oxide precipitates only, and using s to denote the volume fraction of insoluble products $\frac{\varepsilon_{prod}}{\varepsilon_0}$ at the cutoff voltage, one will obtain,

$$V_{cut}-V_0\frac{RT}{(1-\beta)F}\left[\tau_a\ln(1-S_{\max})+(1-\beta)\ln\left(\frac{1-\frac{3}{4}\frac{Da}{\varepsilon^{\tau_d-\tau_{d,o}}(1-S_{\max})^{\tau_d}}}{1-\frac{3}{4}\frac{Da}{\varepsilon^{\tau_d-\tau_{d,o}}}}\right)\right] \tag{18}$$

Rearrangement will lead to

$$(1-S_{\max})^{\tau_a}\left(\frac{1-\mathrm{Da}\frac{3}{4(1-S_{\max})^{\tau_d}}}{1-\frac{3}{4}\mathrm{Da}}\right)^{1-\beta}=e^{\frac{(1-\beta)F(V_{cut}-V_0)}{RT}} \tag{19}$$

The above requires numerical iterative methods to solve. To obtain approximate analytic solutions, two regimes are defined through the below two asymptotes, $s_{max,a}$ and $s_{max,d}$:

$$s_{max,a}=1-e^{\frac{(1-\beta)F(V_{cut}-V_0)}{RT\tau_a}} \tag{20}$$

$$s_{max,d}=1-\left[\frac{3}{4}\frac{\mathrm{Da}}{1-\left(1-\frac{3}{4}\mathrm{Da}\right)e^{\frac{F(V_{cut}-V_0)}{RT}}}\right]^{\frac{1}{\tau_d}} \tag{21}$$

In Regime #1, the exact s_{max} is approximated by $s_{max,a}$, i.e. the electrode passivation solely drops the battery voltage to the cut-off voltage. It can be seen that $s_{max,a}$ is determined by the coverage factor, τ_a. In this regime, $s_{max,a} < s_{max,d}$. In Regime #2, the exact s_{max} is approximated by $s_{max,d}$, i.e. the oxygen transport polarization alone decreases the battery voltage to the cut-off voltage. It can be seen that $s_{max,d}$ is closely related to the tortuosity, τ_d. In this Regime, $s_{max,a} > s_{max,d}$. To determine the above two regimes, one can establish the relationship between τ_a and τ_d. For Regime #1, by using $s_{max,a} \leq s_{max,d}$ one will obtain

$$\frac{\tau_d}{\tau_a} \geq \frac{RT}{(1-\beta)F(V_{cut}-V_0)} \ln\left(\frac{3}{4}\frac{Da}{1-e^{\frac{F(V_{cut}-V_0)}{RT}}}\right) \tag{22}$$

and vice versa for Regime #2. More detailed discussion will be presented in Figs. 4 and 5.

Charge capacity: Charge capacity is an important parameter that characterizes battery performance. For a constant discharge current, one can have

$$Q = \int_0^{t_{max}} I\, dt = It_{max} \tag{23}$$

where t_{max} is the discharge duration of the battery till the cut-off voltage, and related to the maximum deposit volume fraction:

$$t_{max} = \frac{n\delta F \rho_{prod}}{IM_{prod}} s_{max}\varepsilon_0 \tag{24}$$

Then,

$$Q = \frac{n\delta F \rho_{prod}}{M_{prod}} s_{max}\varepsilon_0 \tag{25}$$

Energy capacity (u): Energy capacity is defined as the total energy produced during discharging operation. It can be obtained by integrating the power over time. Under a constant current *I*, one will obtain

$$u = IV_0\, t_{max} + I\int_0^{t_{max}} \Delta\eta\, dt \tag{26}$$

Substituting t_{max} in Eq. (23) will yield

$$u = V_0 \frac{n\delta F \rho_{prod}}{M_{prod}} S_{max}\varepsilon_0 + I\int_0^{t_{max}} \Delta\eta\, dt \tag{27}$$

The integral term on the right can be rewritten as,

$$I\int_0^{t_{max}} \Delta\eta\, dt = I\int_0^{t_{max}} \frac{RT}{(1-\beta)F}\left[\tau_a \ln(1-s) + (1-\beta)\ln\left(1 - Da\frac{3}{4}\frac{1}{(1-s)^{\tau_d}}\right)\right] dt \tag{28}$$

Given that

$$dt = \frac{n\delta F \rho_{prod}\varepsilon_0}{IM_{prod}} ds \tag{29}$$

one will further obtain

$$I\int_0^{t_{max}} \Delta\eta\, dt = \frac{RTn\delta\rho_{prod}\varepsilon_0}{M_{prod}(1-\beta)} \int_0^{s_{max}} \tau_a \ln(1-s) + (1-\beta)\ln\left(1 - Da\frac{3}{4}\frac{1}{(1-s)^{\tau_d}}\right) ds \tag{30}$$

Because the voltage loss leads to capacity decrease, one can express the energy capacity as below

$$u = u_0 - \Delta u_a - \Delta u_d \tag{31}$$

where

$$u_0 = V_0 \frac{n\delta F \rho_{prod}}{M_{prod}} s_{max}\varepsilon_0$$

$$\Delta u_a = -\frac{RTn\delta\rho_{prod}\varepsilon_0}{M_{prod}(1-\beta)} \int_0^{s_{max}} \tau_a \ln(1-s) ds = \frac{RTn\delta\rho_{prod}\varepsilon_0}{M_{prod}(1-\beta)} [s_{max} + (1-s_{max})\ln(1-s_{max})]$$

$$\Delta u_d = -\frac{RTn\delta\rho_{prod}\varepsilon_0}{M_{prod}(1-\beta)} \int_0^{s_{max}} (1-\beta)\ln\left(1 - Da\frac{3}{4}\frac{1}{(1-s)^{\tau_d}}\right) ds$$

It will be extremely difficult to extract an analytic solution from the above integral for Δu_d. In experiment, it is shown that the voltage loss associated with oxygen transport and precipitates is only important in the very short duration near the cut-off voltage. Thus, an approximate solution can be achieved by neglecting Δu_d, to be discussed in a latter section, which will yield an approximate expression for u:

$$u = V_0 \frac{n\delta F \rho_{prod}}{M_{prod}} s_{max}\varepsilon_0 - \frac{RTn\delta\rho_{prod}\varepsilon_0}{M_{prod}(1-\beta)} [s_{max} + (1-s_{max})\ln(1-s_{max})] \tag{32}$$

Note that s_{max} is approximated by $s_{max,a}$ *in* regime #1 and $s_{max,d}$ in regime #2, given by Eqs. (20) and (21), respectively.

In the above derivation, we assume battery continuously operates till the cut-off voltage. For intermittent operation which was reported to benefit Li-air battery performance by relieving oxygen transport [44], the enhanced availability of oxygen needs to be taken into account in the modeling and formula in order to predict the battery capacity.

3. Experimental

To validate the analytical solutions, experiment was conducted over a wide range of cathode materials, including carbon materials, binders, and various electrolytes. Details regarding the experiment was explained in Ref. [9]. In below we briefly describe the cathode fabrication, electrolyte preparation, and cell construction/testing method.

Air Cathode Fabrication: Acetone, specific carbon material, PVDF, and dibutyl phthalate were mixed and stirred sufficiently to make cathode slurries. Several carbon materials were used, including Raven 760 Beads, Raven 890 Powder, and Raven 22 Powder from Columbian Chemicals, ABG1010 from Superior Graphite, Super P from MMM Carbons, and MCMB 10–28 from Osaka Gas, which were used as received. Then the acetone slurries were coated on a glass plate to form cathode films. The cathode films were dried under vacuum at 100 C for a minimum of 2 h with a thickness ranging from 225 μm to 315 μm and densities ranging from 0.4 to 1.3 g/cm^3. In battery testing, the dried cathode films were cut into 5 cm^2 pieces and laminated to aluminum grids treated with a carbon/binder mixture that insures low grid to cathode contact resistance. The dibutyl phthalate was removed from the laminated cathode by extraction in methanol. Acetylene Black-PTFE air cathodes were prepared by Gore in a proprietary process to be either standard density (0.38 g/cm^3) or low density (0.213 g/cm^3).

Electrolyte Preparation: Propylene carbonate (PC), 1,2-dimethoxyethane (DME), and dioxolane (DOL) from Ferro

Corporation were used as received. All solvents and solvent mixtures were tested on a Karl Fisher titrator and were determined to contain less than 20 ppm water before use. Hashimoto $LiPF_6$ salt was used to prepare electrolyte solutions. Electrolyte preparation was conducted in a glovebox with <5 ppm oxygen and <1 ppm water.

Pouch Cell Construction and Testing: Cells were designed to be cathode limited with a nickel tab used for the anode collector and an aluminum tab for the cathode collector. Cells were constructed by placing a dried cathode, non-woven polypropylene separator and a lithium foil pressed onto nickel grid, onto a 5 cm^2 polypropylene block. The cathode/separator/anode assembly was bound to the polypropylene block using insulated nickel wires. Cells were placed in foil laminate pouches with 4 g of electrolyte added. 100 ml of ultrapure carrier (UPC) grade O_2 was then sealed into the pouch. In testing, cells were discharged at rates of 0.05, 0.02, 0.01 mA/cm^2, respectively, to 2 V at ambient temperature. In addition, the experiment and Li-air batteries are designed to validate the developed formula. Thus, cycling performance, which is beyond the scope of this study, was not investigated in the experiment.

4. Results and discussion

Fig. 2 compares the model prediction by Eq. (13) with experimental data under two current densities, 0.08 mA/ cm^2 and 0.24 mA/cm^2. The physical properties and model parameters for this comparison are listed in Table 1. Acceptable agreements are achieved for the two current densities. It can be seen the discharge voltage evolution experiences an initial slow decrease, followed by a fast drop in the latter stage. The initial stage of decrease is primarily caused by the electrode passivation and surface reduction due to the insoluble discharge precipitates in the cathode. As to the latter stage, the fast drop is primarily due to the pore network clogging due to precipitates, which hampers oxygen access to the reaction site.

Fig. 3 plots $\Delta\eta_a$ and $\Delta\eta_d$ as a function of the deposit volume fraction in the validation of Fig. 2. Their physical meanings are the voltage losses caused by the two mechanisms: $\Delta\eta_a$ arises from the electrode passivation and surface reduction, while $\Delta\eta_d$ is caused by the oxygen transport clogging. It can be seen that for the majority

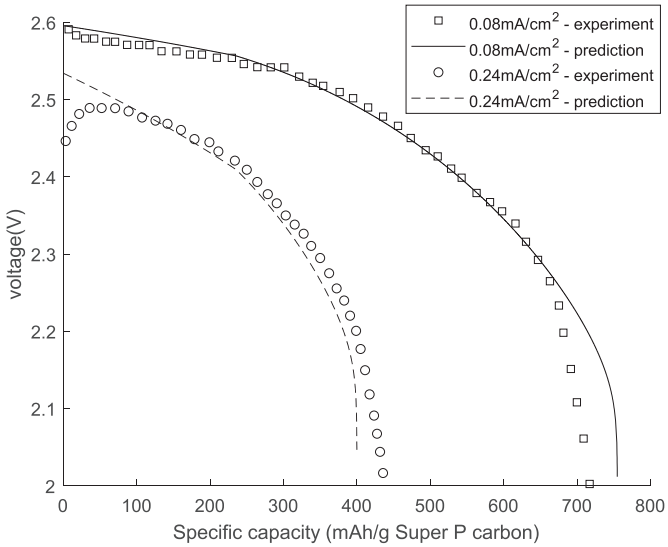

Fig. 2. Comparison of the output voltage prediction with experimental data [32]. The experiment was conducted on a Li-air battery using a PVDF/Super P/NMP cathode.

Table 1
Physical properties and model parameters [23, 31,32].

Parameter	Unit	Value
Temperature	K	298
Transfer Coefficient β	–	0.5
Faraday Constant	C/mol	96,485
O_2Diffusivity in Electrolyte	m^2/s	1.83×10^{-9}
O_2Concentration	Mol/m^3	3.98
Tortuosity τ	–	1.8
Electrode Porosity	–	0.878
Electrode Thickness	mm	1.17
Molecular Weight Li_2O_2	Kg/mol	0.04588
Molecular Weight Li_2O	Kg/mol	0.02988
Molecular Weight Li_2CO_3	Kg/mol	0.07389
I_0	A/m^2	0.6
B_1	–	2.5
B_2	–	8
S_0	–	0.2

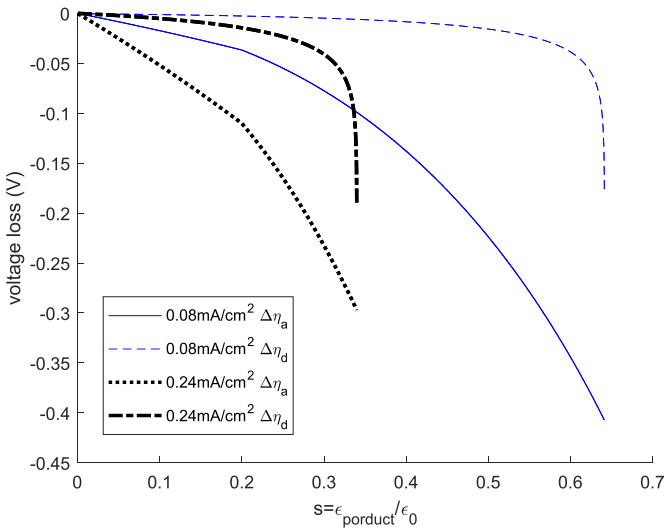

Fig. 3. $\Delta\eta_a$ and $\Delta\eta_d$ as a function of the precipitate volume fraction in the validation of Fig. 2 [32]. η_a arises from electrode passivation and surface reduction, while $\Delta\eta_d$ is caused by oxygen transport clogging.

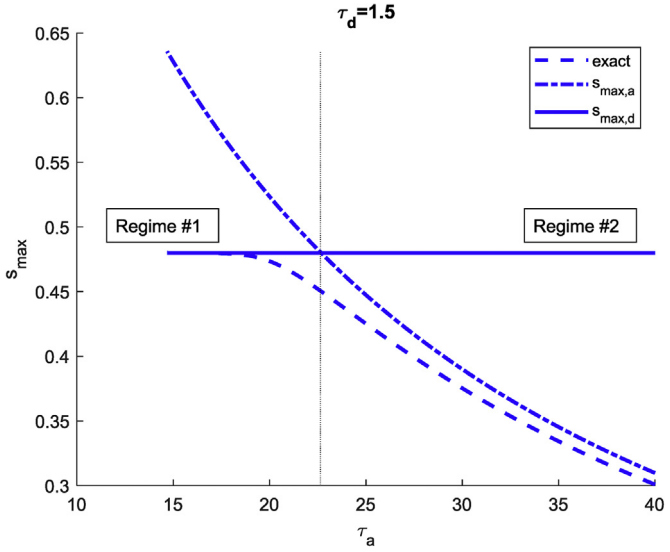

Fig. 4. Comparison of s_{max} from Eq. (19), $s_{max,a}$ from Eq. (20), and $s_{max,d}$ from Eq. (21) as a function of the surface coverage factor. Regime #1 is defined for $s_{max,a} \geq s_{max,d}$. Regime #2 is defined for $s_{max,d} > s_{max,a}$. The maximum error is 6.88% between s_{max} and $s_{max,a}$ or $s_{max,d}$.

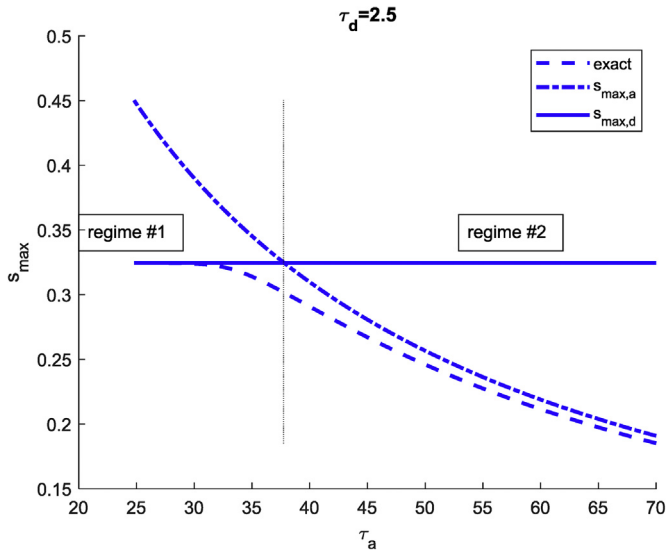

Fig. 5. Comparison of s_{max}, $s_{max,a}$, and $s_{max,d}$ under τ_d of 2.5. Regime #1 is defined for $s_{max,a} \geq s_{max,d}$. Regime #2 is defined for $s_{max,d} > s_{max,a}$. The maximum error is 7.63% between s_{max} and $s_{max,a}$ or $s_{max,d}$.

duration of the discharge operation, electrode passivation and surface reduction are responsible for the voltage loss. Only near the end of discharge does the voltage loss associated with oxygen transport become significant.

Fig. 4 plots the exact solution of s_{max} solved by Eq. (19) numerically using an iterative method, in comparison with the two asymptotes $s_{max,a}$ and $s_{max,d}$ *by* Eq. (20) and (21)*, respectively*. In the figure, Regime #1 is labeled for $s_{max,a} \geq s_{max,d}$, while Regime #2 for $s_{max,d} > s_{max,a}$. It can be seen that asymptotes provide fairly accurate predictions for both Regime #1 and Regime #2. The maximum difference from the exact one is 6.9% near the across point of the two asymptotes. Note that $s_{max,d}$ is independent of τ_a, thus a horizontal line is plotted in comparison with the other two curves. Fig. 5 shows the same result but with $\tau_d = 2.5$, also indicative of a good approximation with an error smaller than 7.6%. In summary, in the range of parameters the two asymptotes provide good approximations to s_{max}. Because $s_{max,a}$ and $s_{max,d}$ are directly expressed, the analytical solutions to the charge capacity and energy capacity can be developed by using the asymptotes for s_{max}.

Fig. 6 plots the two energy capacity losses in Eq. (31) for 0.08 mA/cm^2 and 0.24 mA/cm^2 in the validation of Fig. 2. The dashed line denotes the loss due to the electrode passivation and surface loss. The dash-dot line represents the loss due to the oxygen transport resistance. It can be seen that Δu_d is much smaller than Δu_a in the two cases. Thus, one can neglect the former loss in the energy capacity analysis.

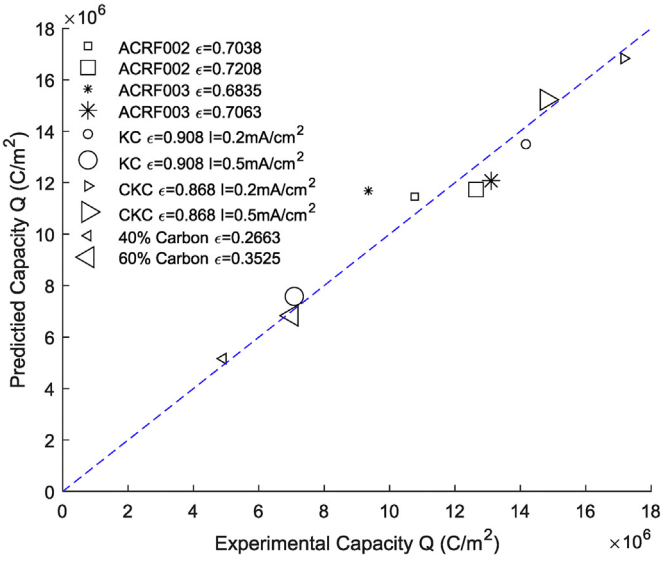

Fig. 7. Comparison of capacity between model prediction and experimental data in the literature, listed in Table 3.

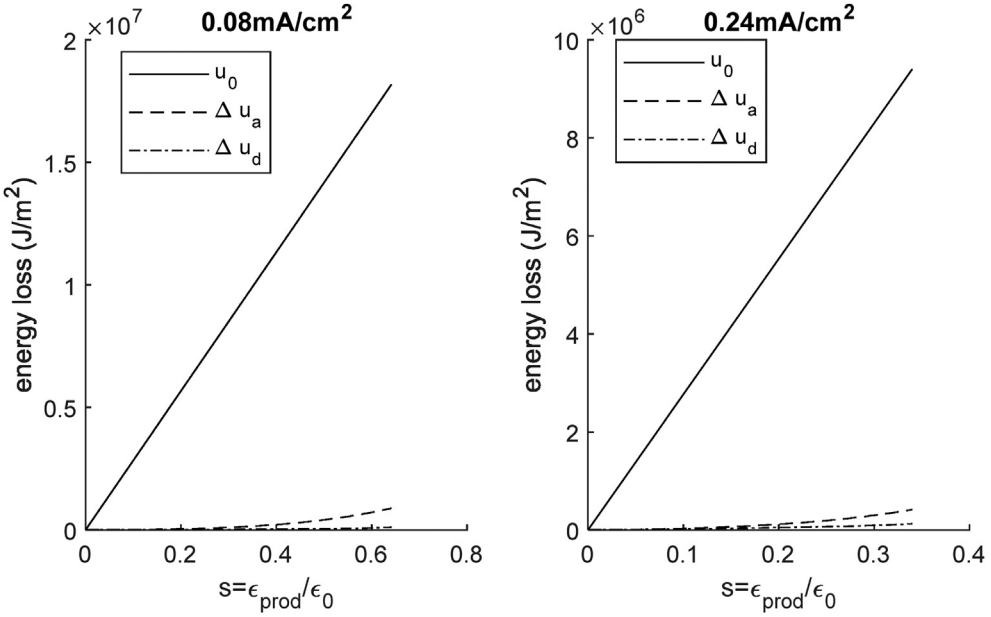

Fig. 6. Two energy losses as a function of s in Eq. (31) in the validation of Fig. 2. The solid line represents u_0 as a reference. u_a arises from electrode passivation and surface reduction. Δu_d is caused by oxygen transport clogging.

Table 2
MacMullin number (N_M) of a system consisting of a dispersed non-conducting phase in a conductive medium [36].

Structure	Particle morphology	Particle arrangement	Size distribution	MacMullin number
I	Spheres	Random	Uniform	$N_M = \frac{(5-\varepsilon)(3+\varepsilon)}{8(1+\varepsilon)\varepsilon}$
II	Spheres	Cubic lattice	Uniform	$N_M = \frac{(3-\varepsilon)\left[\frac{4}{3}+0.409(1-\varepsilon)^{7/3}\right]-1.315(1-\varepsilon)^{10/3}}{2\varepsilon\left[\frac{4}{3}+0.409(1-\varepsilon)^{7/3}\right]-1.315(1-\varepsilon)^{10/3}}$
III	Spheres	Random and ordered	Range	$N_M = \varepsilon^{-1.5}$
IV	Cylinders	Parallel (square array)	Uniform	$N_M = \frac{2-\varepsilon-0.3058(1-\varepsilon)^4-1.334(1-\varepsilon)^8}{\varepsilon-0.3058(1-\varepsilon)^4-1.334(1-\varepsilon)^8}$
V	Fibrous material (Cylinders)	Random	–	$N_M = \frac{0.9126}{\varepsilon(\varepsilon-0.11)^{0.785}}$

Table 3
Literature experimental data for validation of Fig. 7.

Cathode carbon	Porosity or density	Active carbon (Wt%)	Measured capacity (mAh/g)	Rate	Binder	Electrolyte
ACRF002-1123 K [46]	1.320 cm^3/g	–	630	20 mA/g	Kynar	1M LiPF6 PC
ACRF002-1273 K [46]	1.282 cm^3/g	–	740	20 mA/g	Kynar	1M LiPF6 PC
ACRF003-1073 K [46]	1.200 cm^3/g	–	528	20 mA/g	Kynar	1M LiPF6 PC
ACRF003-1123 K [46]	1.336 cm^3/g	–	880	20 mA/g	Kynar	1M LiPF6 PC
KC [47]	91%	90%	761/430	0.2/0.5 mA/cm^2	PTFE	0.2M LiTriflate PC:TFP (7:3)
CKC [47]	87%	90%	817/597	0.2/0.5 mA/cm^2	PTFE	0.2M LiTriflate PC:TFP (7:3)
40% C [48]	0.121 cm^3/g	40%	306	80 mA/g	Kynar	1M LiPF6 PC
60% C [48]	0.140 cm^3/g	60%	615	80 mA/g	Kynar	1M LiPF6 PC

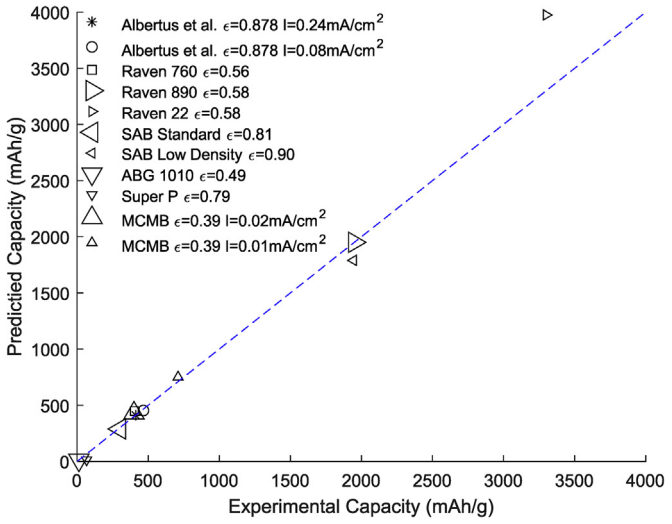

Fig. 8. Comparison of capacity between model prediction and our experiment in Table 4 and Albertus et al. [32].

Fig. 7 shows the comparison of the discharge capacity between the prediction and experimental data reported in the literature for various cathode configurations, porosity/density, and materials. Details regarding the experimental data are listed in Table 3. In the experiments, the discharging products vary depending on the electrolyte materials. For example, electrolytes of carbonate-based solvents likely have Li_2CO_3 as discharging product. Thus, the values of M_{prod} and n will change in the model prediction [31,32]. For cathodes of the same material and porosity, all the modeling parameters, including the surface area, tortuosity, cathode thickness, discharge product properties, and surface coverage factor, are set the same, except the discharge current density and V_0. A good agreement is indicated by the figure. Fig. 8 shows the comparison with our experimental data, along with the data in the validation of Fig. 2. In the experiment, because of different carbon materials and binders used in the fabrication, the cathode porosity ranges from 39% to 90%. Experimental detail is given in Table 4. Again, a good agreement is indicated by the figure. In addition, many electrolyte materials have been investigated for Li-air battery application, including the ones listed in Tables 3 and 4. It also reported that DME and DOL were oxidized at the presence of oxygen [45]. The analytical formula are targeted at the effects of insoluble Li oxides, which is less related to electrolyte selection and decomposition.

Table 4
Experimental data of cathode and electrolyte materials and battery capacity for validation of Fig. 8.

Cathode carbon	Cathode density (g/cm^3)	Porosity	Active carbon (Wt%)	Measured capacity (mAh/g)<	Rate (mA/cm^2)	Binder	Electrolyte
Raven 760	0.848	56%	50%	412	0.05	Kynar	1M LiPF6 PC:DME (1:1)
Raven 890	0.811	58%	50%	466	0.05	Kynar	1M LiPF6 PC:DME(1:1)
Raven 22	0.822	58%	50%	405	0.05	Kynar	1M LiPF6 PC:DME(1:1)
ABG1010	0.987	49%	50%	300	0.05	Kynar	1M LiPF6 PC:DME(1:1)
Super P	0.401	79%	50%	1944	0.05	Kynar	1M LiPF6 PC:DME(1:1)
SAB standard	0.380	81%	80%	1950	0.05	PTFE	1M LiTriflate DOL:DME(1:1)
SAB low density	0.213	90%	80%	3300	0.05	PTFE	1M LiTriflate DOL:DME(1:1)
MCMB	1.268	39%	76%	12.2/66.7	0.02/0.01	Kynar	1M LiTriflate DOL:DME(1:1)

Thus, the approximate formula can be extended to other electrolytes. Additionally, carbon is used as cathode material in the experiments of Figs. 7 and 8. The approximate formula can be extended to other materials by using the corresponding parameters such as the exchange current density, porosity, surface coverage factor, and tortuosity. Furthermore, in each of Figs. 7 and 8 there exists one data point with a large error (about 20–25% deviation). It is possibly due to uncertainty in experiment, e.g. impurity in materials and side reactions, or other factors that the model doesn't taken into account, e.g. electrolyte decomposition. In general, 20–25% deviation is acceptable for analytical approximation.

5. Conclusion

In this work, we presented a modeling analysis on the discharge operation of nonaqueous Li-air batteries and obtained approximate solutions for the maximum insoluble product storage capacity and the losses of discharge capacity and energy capacity caused by insoluble precipitates. Approximate solutions explicitly express the maximum volume fraction of insoluble precipitates, discharge capacity, and energy capacity as a function of material properties, cathode structure, and model parameters. Two regimes were defined by the dominant mechanisms of the voltage loss. It was found that s_{max} can be approximated by the two asymptotes with errors less than 8% for both Regimes #1 and 2, respectively. The boundary of the two regimes can be identified through the ratio of the surface coverage factor and tortuosity. Further, the approximate solutions of charge and energy capacity loss were obtained. Explicit expression was achieved for energy capacity estimate when the contribution from the oxygen transport loss is negligible. The approximations were extensively validated against various experimental data, including literature reported and in-house testing results in a wide range of cathode materials of carbon and binders, and in the range of porosity from 39% to 91%. The developed analytical solutions can also be directly applied to optimize battery capacity, control, and hybrid optimization with other renewable power.

Acknowledgment

We gratefully acknowledge the support of the National Science Foundation (CBET-1336873) on this study.

References

[1] K.M. Abraham, Z. Jiang, J. Electrochem. Soc. 143 (1) (1996) 1–5.
[2] G. Girishkumar, B. McCloskey, A. Luntz, S. Swanson, W. Wilcke, J. Phys. Chem. Lett. 1 (2010) 2193–2203.
[3] P.G. Bruce, S.A. Freunberger, L.J. Hardwick, J.M. Tarascon, Nat. Mater. 11 (2012) 19–29.
[4] J.S. Lee, S.T. Kim, R. Cao, N.S. Choi, M. Liu, K.T. Lee, J. Cho, Adv. Energy Mater. 1 (2011) 34–50.
[5] Z. Wen, C. Shen, Y. Lu, ChemPlusChem 80 (2) (2015) 270.
[6] S.J. Visco, V.Y. Nimon, A. Petrov, K. Pridatko, N. Goncharenko, E. Nimon, L.D. Jonghe, Y.M. Volfkovich, D.A. Bograchev, J. Solid State Chem. 18 (2014) 1443.
[7] T. Ogasawara, A. Débart, M. Holzapfel, P. Novák, P.G. Bruce, J.A. Chem, For. Soc. 128 (2006) 1390–1393.
[8] J. Read, J. Electrochem. Soc. 149 (2002) A1190–A1195.
[9] T. Kuboki, T. Okuyama, T. Ohsaki, N. Takami, J. Power Sources 146 (2005) 766–769.
[10] H. Cheng, K. Scott, J. Power Sources 195 (2010) 1370–1374.
[11] C.O. Laoire, S. Mukerjee, K.M. Abraham, E.J. Plichta, M.A. Hendrickson, J. Phys. Chem. C 114 (2010) 9178–9186.
[12] Y. Wang, S.C. Cho, J. Electrochem. Soc. 160 (10) (2013) A1847.
[13] Y. Wang, H. Yuan, J. Electrochem. Soc. 164 (9) (2017) A2283–A2289.
[14] J. Yuan, J.-S. Yu, B. Sunden, J. Power Sources 278 (27) (2015) 352.
[15] K. Yoo, S. Banerjee, P. Dutta, J. Power Sources 258 (2014) 340.
[16] V. Viswanathan, K.S. Thygesen, J.S. Hummelshøj, J.K. Nørskov, G. Girishkumar, B.D. McCloskey, A.C. Luntz, J. Chem. Phys. 135 (2011) 214704.
[17] U. Sahapatsombut, H. Cheng, K. Scott, J. Power Sources 249 (2014) 418.
[18] S.S. Sandhu, J.P. Fellner, G.W. Brutchen, J. Power Sources 164 (2007) 365.
[19] Y. Inaguma, M. Nakashima, J. Power Sources 228 (2013) 250.
[20] F. Ghamouss, M. Mallouki, B. Bertolotti, L. Chikh, C. Vancaeyzeele, S. Alfonsi, O. Fichet, J. Power Sources 197 (2012) 267.
[21] L. Puech, C. Cantau, P. Vinatier, G. Toussaint, P. Stevens, J. Power Sources 214 (2012) 330.
[22] X.J. Chen, V.V. Bevara, P. Andrei, M. Hendrickson, E.J. Plichta, J.P. Zheng, J. Electrochem. Soc. 161 (2014) A1877.
[23] J. Christensen, P. Albertus, R.S. Sanchez-Carrera, T. Lohmann, B. Kozinsky, R. Liedtke, J. Ahmed, A. Kojic, J. Electrochem. Soc. 159 (2012) R1.
[24] E.J. Nemanick, J. Power Sources 247 (2014) 26.
[25] M. Yuasa, T. Matsuyoshi, T. Kida, K. Shimanoe, J. Power Sources 242 (2013) 216.
[26] P. Andrei, J.P. Zheng, M. Hendrickson, E.J. Plichta, J. Electrochem. Soc. 157 (2010) A1287.
[27] Y. Wang, K.S. Chen, J. Mishler, S.C. Cho, X.C. Adroher, Appl. Energy 88 (2011) 981–1007.
[28] Y. Wang, K.S. Chen, S.C. Cho, PEM Fuel Cells: Thermal and Water Management Fundamentals, Momentum Press, 2013.
[29] R.M. LaFollette, D.N. Bennion, J. Electrochem. Soc. 137 (1990) 3701–3707.
[30] C.Y. Wang, W.B. Gu, B.Y. Liaw, J. Electrochem. Soc. 145 (1998) 3407–3417.
[31] Y. Wang, Electrochim. Acta 75 (2012) 239.
[32] P. Albertus, G. Girishkumar, B. McCloskey, R.S. Sanchez-Carrera, B. Kozinsky, J. Christensen, A.C. Luntz, J. Electrochem. Soc. 158 (3) (2011) A343.
[33] Y. Wang, J. Electrochem. Soc. 154 (2007) B1041.
[34] B. Tjaden, S.J. Cooper, D.J. Brett, D. Kramer, P.R. Shearing, Curr. Opin. Chem. Eng. 12 (2016) 44–51.
[35] Y. Wang, C.-Y. Wang, K.S. Chen, Electrochim. Acta 52 (12) (2007) 3965–3975.
[36] Y. Wang, Z. Wang, H. Yuan, T. Li, Electrochim. Acta 180 (2015) 382–393.
[37] J. Newman, K.E. Thomas-Alyea, Electrochemical Systems, 3 ed., John Wiley & Sons, New York, 2004.
[38] J. Newman, W. Tiedemann, AIChE J. 21 (1975) 25–41.
[39] Y. Wang, S.C. Cho, J. Electrochem. Soc. 160 (10) (2013) A1–A9.
[40] Y.C. Lu, H.A. Gasteiger, Y. Shao-Horn, Catalytic activity trends of oxygen reduction reaction for nonaqueous Li-air batteries, J. Am. Chem. Soc. 133 (47) (2011) 19048–19051.
[41] X. Wang, X. Hou, Q. Wang, W. Ge, S. Guo, In situ fabrication of flaky-like NiMn-layered double hydroxides as efficient catalyst for Li-O 2 battery, J. Solid State Electrochem. 23 (4) (2019) 1121–1128.
[42] H. Liu, M. Liu, L. Yang, Y. Song, X. Wang, K. Yang, F. Pan, A bi-functional redox mediator promoting the ORR and OER in non-aqueous Li–O 2 batteries, Chem. Commun. 55 (46) (2019) 6567–6570.
[43] M. Song, H. Tan, X. Li, A.I.Y. Tok, P. Liang, D. Chao, H.J. Fan, Atomic-layer-deposited amorphous MoS2 for durable and flexible Li–O2 batteries, Small Methods (2019) 1900274.
[44] D. Zhu, L. Zhang, M. Song, X. Wang, R. Mi, H. Liu, Y. Chen, Intermittent operation of the aprotic Li-O2 battery: the mass recovery process upon discharge interval, J. Solid State Electrochem. 17 (9) (2013) 2539–2544.
[45] D. Zhu, L. Zhang, M. Song, X. Wang, J. Mei, L.W. Lau, Y. Chen, Solvent autoxidation, electrolyte decomposition, and performance deterioration of the aprotic Li-O 2 battery, J. Solid State Electrochem. 17 (11) (2013) 2865–2870.
[46] M. Mirzaeian, P.J. Hall, Electrochim. Acta 54 (28) (2009) 7444–7451.
[47] X. Ren, S.S. Zhang, D.T. Tran, J. Read, J. Mater. Chem. 21 (2011) 10118–10125.
[48] S.R. Younesi, S. Urbonaite, F. Björefors, K. Edström, J. Electrochem. Soc. 22 (2011) 9835–9838.
[49] Y. Wang, D.F.R. Diaz, K.S. Chen, Z. Wang, X.C. Adroher, Materials, technological status, and fundamentals of PEM fuel cells–a review, Mater. Today (2019), https://doi.org/10.1016/j.mattod.2019.06.005. In press.